Supporting Information

All-dielectric Meta-optics for High-Efficiency Independent Amplitude and Phase Manipulation

Brian O. Raeker, Hanyu Zheng, You Zhou, Ivan I. Kravchenko, Jason Valentine, and Anthony Grbic**

B.O. Raeker, A. Grbic*
Department of Electrical Engineering and Computer Science, University of Michigan, Ann Arbor, MI, 48109 USA
Email address: agrbic@umich.edu
*Corresponding author

H. Zheng
Department of Electrical Engineering and Computer Science, Vanderbilt University, Nashville, TN, 37212 USA

Y. Zhou
Photonics Initiative, Advanced Science Research Center, City University of New York, New York, NY, 10031, USA

I.I. Kravchenko
Center for Nanophase Materials Sciences, Oak Ridge National Laboratory, Oak Ridge, Tennessee 37831, USA

J. Valentine*
Department of Mechanical Engineering, Vanderbilt University, Nashville, TN, 37212 USA
Email address: jason.g.valentine@vanderbilt.edu
*Corresponding author

Supplementary Note 1: Unit Cell Design

1.1 Simulation of Unit Cell vs. Dimensions

Each compound meta-optic is composed of two metasurfaces applying a polarization-independent phase profile onto the incident wave. The metasurfaces are implemented as arrays of high dielectric contrast nanopillars, which locally provide the desired transmission phase shift by varying the diameter of the nanopillars across the metasurface. Figure S1(a) shows a schematic of the metasurface unit cell and the relevant dimensions. The unit cell dimensions can be varied to achieve a desired transmission profile as a function of pillar diameter. In this case, a large phase coverage with high transmission magnitude is desired. To find the desired pillar dimensions, simulations of the metasurface unit cell (with Floquet boundary conditions to simulate a periodic array) were performed to determine the transmission magnitude as a function of the pillar diameter and the period, pillar height, or wavelength (see Figure S1(b)-(d)). The transmission phase will change as the pillar diameter changes, so dimensions are sought which maximize transmission magnitude.

Figure S1(b)-(d) show that a high transmission magnitude as a function of diameter can be achieved for a unit cell period of $p = 570$nm, pillar height of $h = 850$nm, and operating wavelength of $\lambda_0 = 1.3\mu$m. The transmission magnitude and phase are shown in Figure S1(e) for these dimensions. By using pillars with diameters ranging from 125nm to 400nm, a transmission phase coverage of 78% with transmission above 0.93 is achieved. Pillar diameters of 310nm-330nm were skipped in the three-dimensional hologram meta-optic design because low-transmission contours were observed in measurement at these diameters. See Section 11.2 for additional details.

The locally period approximation [2, 3] was used to simplify the design of the metasurfaces. The pillar diameters of the array were determined by matching the desired local transmission to the transmission obtained from periodic simulations of each unit cell. This approximation is commonly used, with resulting metasurface performance largely matching the desired transmission characteristics. The most significant exception is the contour between the smallest-diameter pillars and the largest-diameter pillars, where simulations of the full metasurface show slightly reduced transmission compared to the local-periodic expectation. However, this is a small error in the transmitted field and does not significantly alter the resulting output field of the meta-optic.

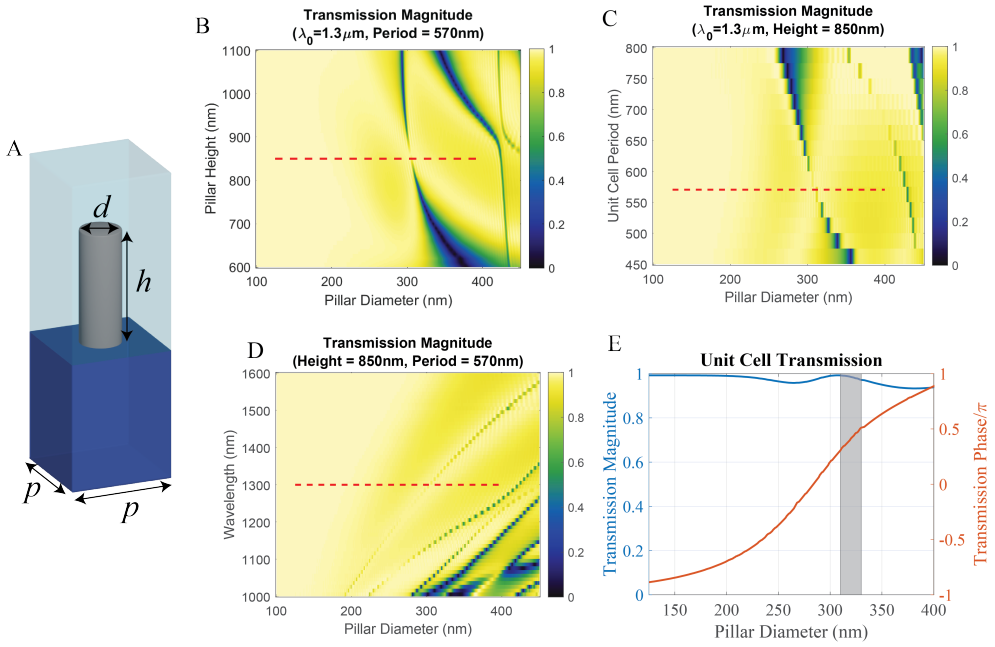

Figure S1: Unit cell geometry and transmission of silicon nanopillars to implement the phase-discontinuous metasurfaces. (A) Diagram of the metasurface unit cell, consisting of an amorphous silicon nanopillar at the boundary of a fused silica and PDMS material interface. The pillars have a height of 850nm and a spacing of 570nm. (B-D) Plots showing the transmission magnitude of the unit cell for variations in dimension around the nominal design, which is marked with a dashed line. (E) Transmission characteristics for the nominal unit cell dimensions while varying the pillar diameter. Diameters of 310nm-330nm are avoided in the hologram design since low transmission was observed in fabricated metasurfaces for these diameters. (Perceptually uniform color bar [1] used for these and all following plots).

1.2 Measurement of Low-Transmission Contours

Pillar diameters of 310nm through 330nm are not used in the metasurface design for the solid image hologram meta-optic (example shown in Figure 5(c-d) of the main text). This is due to low transmission intensity measured over contours on fabricated metasurfaces containing this diameter range, which is lower than the expected full transmission in simulation. A low measured transmission magnitude is an indicator that the phase of the transmitted field also deviates from the expected value. Both errors in the measured transmitted field combine to adversely impact the measured output field of the meta-optic.

This effect was observed in a meta-optic fabricated for a hologram design (different design than those presented in the main text) using the entire 125nm-400nm pillar diameter range. The diameters of the nanopillars constituting metasurface 1 are shown in Figure S2(a). The measured transmitted intensity of this metasurface is shown in Figure S2(b), where low transmission contours are visible. Various contours of different pillar diameter ranges were compared to the measured transmitted intensity to determine which pillars were exhibiting low transmission in measurement. Figure S2(c) shows the contour formed by pillars with diameters of 310nm-330nm overlayed with the transmitted intensity. The nanopillars with diameters of 310nm-330nm align with the low-transmission portions of the metasurface, suggesting that the low transmission occurs for these specific nanopillar diameters.

While the cause of low transmission for these pillar diameters is not explicitly known, it is expected that fabrication errors alter the symmetry of the pillar, which disrupts the resonance behavior to introduce a reduced transmission. For example, it has been shown that asymmetry in high-index contrast structures enables coupling to symmetry-protected modes (also known as bound states in the continuum) to produce sharp transmission or reflection resonances [4, 5, 6]. The simulations assumed perfectly shaped cylinders, so might not have experienced this effect. However, Figure S1(b-c) show that a slight change in pillar height or pillar spacing can cause low transmission for this range of pillar diameters, so it is expected other fabrication errors could have a similar effect.

These low-transmission contours result in phase and amplitude errors in the output field distribution of the meta-optic. The hologram image quality is degraded as a result. This is illustrated in Figure S3, where the effects of the low-transmission contours from each metasurface reduce the quality of the desired output field of the meta-optic. The desired output intensity distribution is shown in Figure S3(a), compared to the measured output intensity in Figure S3(b). The measured intensity exhibits low-intensity contours like the low-transmission contours of metasurface 1. There-

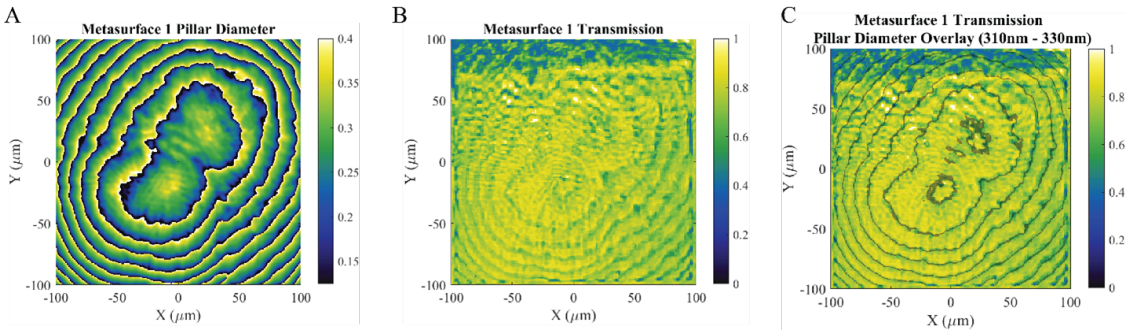

Figure S2: Transmission intensity measurement showing that pillars with diameters of 310nm-330nm give lower transmission. (A) The pillar diameters of the nanopillar array implementing metasurface 1 (scale bar in micron). (B) Measured transmission intensity of the fabricated metasurface. (C) Contours of nanopillars with 310nm-330nm diameters (dark gray bands) overlaid on the measured transmission intensity. These contours match the observe low-transmission contours.

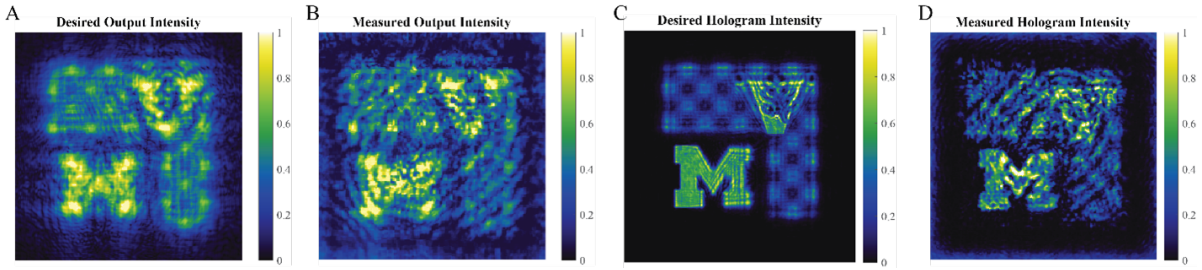

Figure S3: A meta-optic forms a solid-image three-dimensional hologram. The metasurfaces contained nanopillars with diameters in the entire 125nm-400nm range. The low-transmission contours due to nanopillars with diameters of 310nm-330nm introduce errors into the output field distribution of the meta-optic and degrade the quality of the hologram. Intensity distributions are normalized to their maximums. (A) The desired output intensity of the meta-optic. (B) The measured output intensity of the meta-optic. Note the low-transmission contours are like those in Figure S2(b) Figure S2(b). (C) The desired intensity of the hologram at a plane where the left portion of the M is in focus. (D) Measured intensity of the hologram. The low-transmission contours are visible in the hologram image, degrading its quality.

fore, the errors of the transmitted field introduced by the metasurface directly result in output intensity distribution errors. Even though only intensity errors were measured in the output field distribution, it is expected that phase errors are also present.

Due to the amplitude and phase errors in the output field profile, the hologram image is degraded in quality. This is seen when comparing the desired hologram image in Figure S3(c) to the measured image in Figure S3(d). While the general image components are recognizable in the measured image, the low-intensity contours are visible and clearly reduce image quality.

With these results in mind, the three-dimensional hologram was re-designed and fabricated without using nanopillar diameters in the range of 310nm-330nm. The low-transmission contours seen in Figure S2 were mitigated. The measured results are shown in Figure 5(d) of the main text.

These low-transmission contours occur for the beam-splitter and former examples but are not as impactful since this function is measured in the far-field. Introducing output field errors over thin contours creates noise in the plane wave spectrum of the output field distribution. However, as this output field propagates to the far-field, the beam profiles separate from the noise to match the desired profiles. Power is lost to this spectral noise, reducing the efficiency. The measured aperture intensity distribution exhibits thin contours of amplitude errors (see Figure 4 of the main text), but the far-field beam profiles match the expected result.

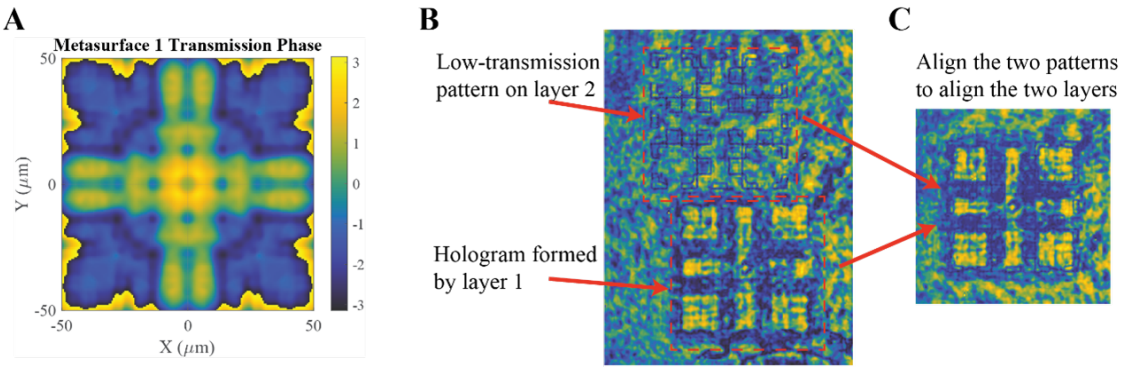

Figure S4: Design and performance of the alignment hologram used to align the two metasurfaces. (A) The phase shift profile of a metasurface which forms the desired hologram at the distance where metasurface 2 should be located. (B) Intensity observed at the plane of the second metasurface. The low-transmission pattern is introduced at the same plane as metasurface 2, while the alignment hologram comes into focus at the desired separation distance from metasurface 1. (C) Aligning the low-transmission pattern with the alignment hologram accurately aligns the two metasurfaces with each other.

Supplementary Note 2: Alignment Hologram

Optimal performance of compound meta-optics requires accurate three-dimensional alignment of the constitutive metasurfaces. Alignment accuracy better than 1.5μm in the x, y directions and 15μm in the z-direction is necessary for adequate performance of multi-metasurface devices. A significant phase error is introduced into the output field when the metasurfaces are misaligned. This phase error alters wave propagation so that the desired function is degraded or no longer achieved. When forming a hologram, increasing the phase error on the output field will distort the hologram image.

We utilize an alignment hologram approach to accurately align the metasurfaces. Nanopillar arrays are placed near the two metasurfaces forming the meta-optic. The array near metasurface 1 was designed using the phase-retrieval algorithm to form a cross-shaped intensity pattern at the desired distance of metasurface 2. As a result, the hologram transfers location information from layer 1 to the same plane as layer 2. The nanopillar array near metasurface 2 contains a pattern of low transmission nanopillars tracing the alignment hologram outline. By positioning layer 2 so that the low-transmission outline is not visible when illuminated by the alignment hologram, the two metasurfaces are accurately aligned.

The nanopillar array forming the alignment hologram is 100μm×100μm in dimension. Figure S4(a) shows the phase shift profile of this array, which forms the intensity hologram in Figure S4(b). The low-transmission outline is aligned with this hologram by adjusting the position of layer 2, as shown in Figure S4(c). This process accurately aligns the two metasurfaces. Small alignment improvements are made by observing the intensity at a distance from the meta-optic output. As the alignment is improved, the phase error on the output field decreases, leading to an intensity image which matches the desired results.

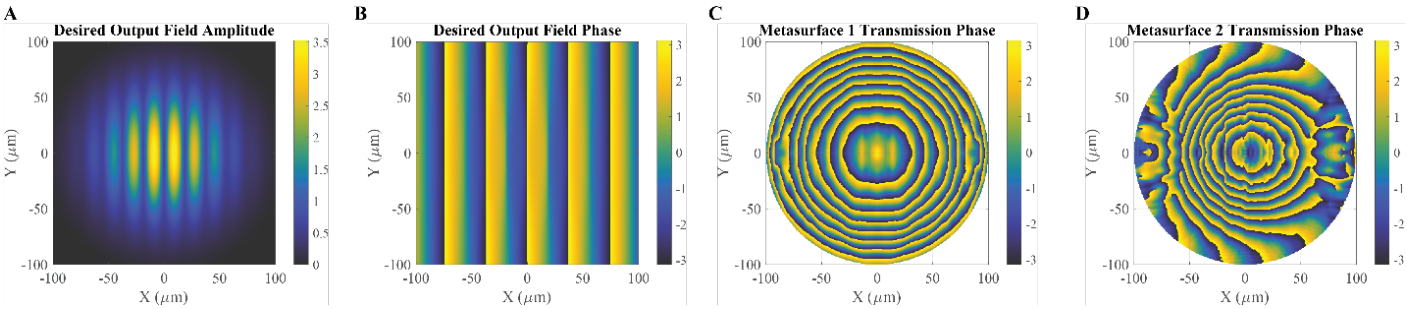

Figure S5: Design of the beam-forming and splitting meta-optic with two beams. (A, B) The amplitude and phase distributions of the desired output field, which is the interference pattern between two Gaussian beams. (C, D) The transmission phase distributions implemented by each metasurface to form the desired field distribution from a circular, uniform illumination.

Supplementary Note 3: Meta-optic Designs

The design of each meta-optic example and full-wave simulation results for each metasurface are given in this section. A finite difference time domain (FDTD) simulation is performed for each metasurface using MEEP [7] (an open-source FDTD solver). The simulated performances of each metasurface are combined [8] using spectral domain methods to obtain the simulated output field of the meta-optic device.

3.1 Combined Beam-forming and Splitting: Two Beams

The first meta-optic example reshapes a circular, uniform illumination to form the interference pattern between two Gaussian beams at the output. Specifically, the output field profile is the direct sum of the two Gaussian beam profiles.

$$E_{out} = -e^{-(r/45.5\lambda_0)^2} e^{ik_0 x \sin(-2^\circ)} + \sqrt{0.5} e^{-(r/32.5\lambda_0)^2} e^{ik_0 x \sin(2^\circ)} \tag{1}$$

The amplitude of the desired output field distribution is shown in Figure S5(a) and the phase in Figure S5(b). The meta-optic design process was used to determine the transmission phase profiles of each metasurface, so the desired field is formed at the output of the device. The resulting transmission phase profiles are shown in Figure S5(c) for metasurface 1 and Figure S5(d) for metasurface 2. These transmission phase profiles are sampled at the unit cell periodicity and translated to a distribution of pillar diameters.

The complete meta-optic design was simulated to verify the device performance. Metasurface 1 was simulated using the field profile of Figure S6(a) as the incident source field. The transmitted field distribution was recorded at a distance of $0.4\lambda_0$ from the metasurface and is shown in Figure S6(b). A phase shift profile has been imparted on the incident field, and high transmission is maintained. This field profile was numerically propagated across the separation distance to the plane containing the second metasurface and is shown in Figure S6(c). This field distribution was used as the source field of the simulation of metasurface 2. The transmitted field distribution of this simulation is shown in Figure S6(d), where a transmission phase shift occurs while maintaining high transmission.

The simulated output field matches the desired output field, showing that the meta-optic design accurately implements the desired complex-valued field conversion from input to output without relying on loss. The simulated output electric field accuracy is demonstrated by calculating the error in the amplitude and phase distributions relative to the desired output field. Figure S7 displays the amplitude and phase error profiles, showing a low error across the meta-optic output.

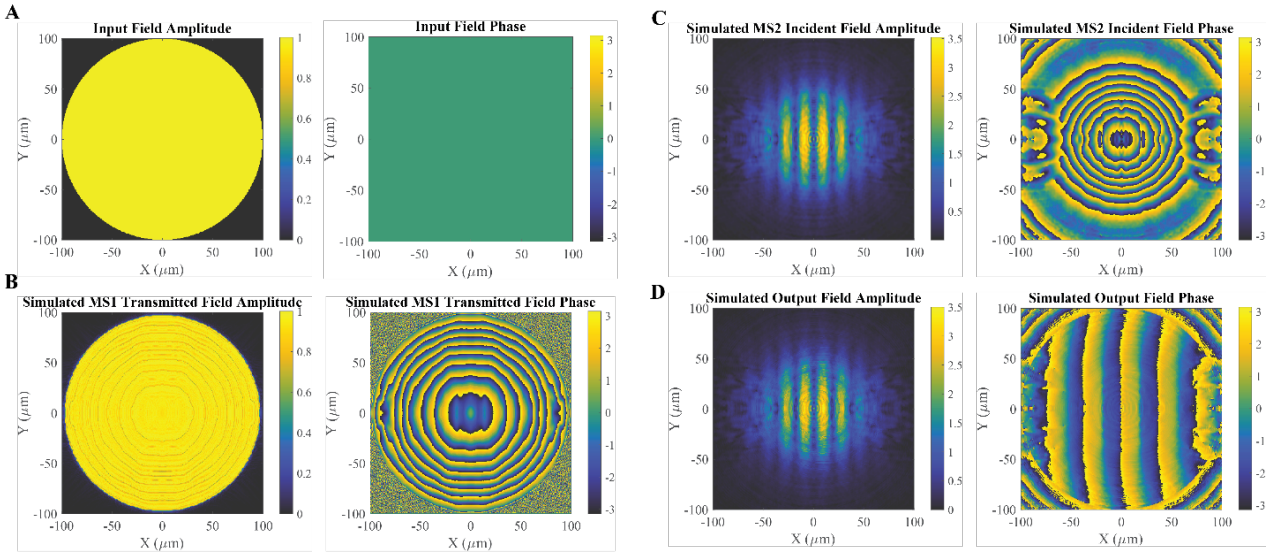

Figure S6: FDTD simulation results of the beam-former and splitter meta-optic example with two beams. (A) The field distribution used as the input to the meta-optic is a circular, uniform illumination. (B) The simulated transmitted field from metasurface 1 shows that the metasurface applies the desired transmission phase shift with high transmission magnitude. (C) The transmitted field from metasurface 1 is numerically propagated to the plane containing metasurface 2. At this plane, the field amplitude distribution matches the desired field amplitude, but the phase is incorrect. (D) The simulated transmitted field from metasurface 2 shows that the metasurface applies the desired transmission phase with high transmission magnitude. This field distribution accurately matches the desired output field, indicating that the meta-optic should perform as expected.

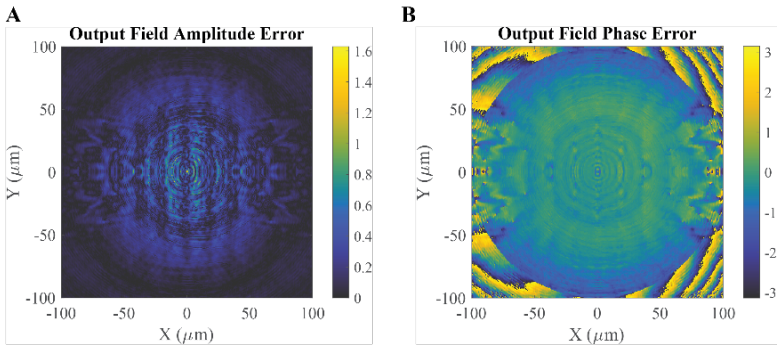

Figure S7: Output field error of the two-beam meta-optic. The amplitude and phase error of the simulated output field relative to the desired output field is low for the two-beam former and splitter example, showing the accuracy of the meta-optic performance. (A) The amplitude error is shown as the root-mean-square error. (B) The phase error of the simulated output field.

3.2 Combined Beam-forming and Splitting: Three beams

The second beam-former and splitter example forms three output Gaussian beams with different peak intensities and propagation directions. The desired output field is calculated as the sum of three beams

$$E_{out} = e^{-(r/45\lambda_0)^2}\left[e^{ik_0[x\sin(2^\circ)+y\sin(0^\circ)]} + \sqrt{0.75}e^{ik_0[x\sin(-1^\circ)+y\sin(3^\circ)]} + \sqrt{0.5}e^{ik_0[x\sin(-2^\circ)+y\sin(-2^\circ)]}\right] \quad (2)$$

The amplitude of the desired output field is shown in Figure S8(a) and the phase in Figure S8(b). The transmission phase profiles of the metasurfaces needed to form the desired output field distribution are given in Figure S8(c, d).

The meta-optic simulation process was performed, with results displayed in Figure S9. Comparing the simulated output field in Figure S9(d) to the desired output field in Figure S8(a, b), we see that the meta-optic design accurately performs the desired complex-valued field conversion. This is further verified by Figure S10 which shows the amplitude and phase error distribution of the simulated output field.

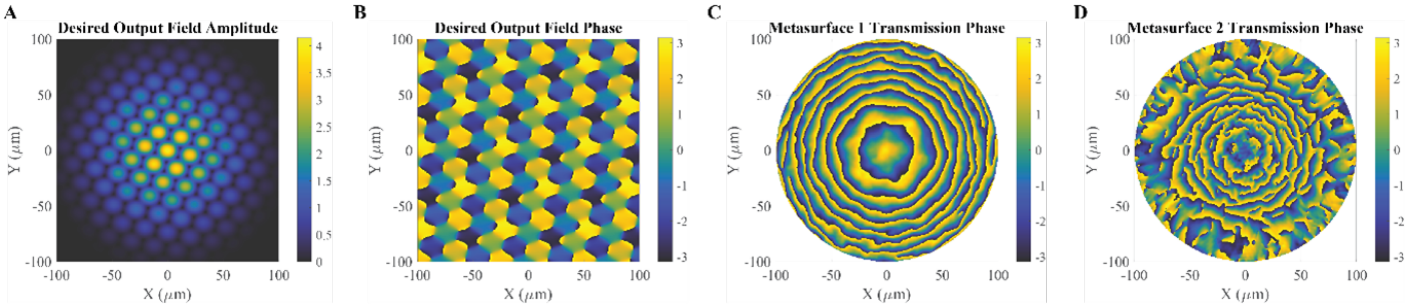

Figure S8: Design of the beam-forming and splitting meta-optic with three beams. (A, B) The amplitude and phase distributions of the desired output field, which is the interference pattern between three Gaussian beams. (C, D) The transmission phase distributions implemented by each metasurface to form the desired output field from the uniform, circular illumination.

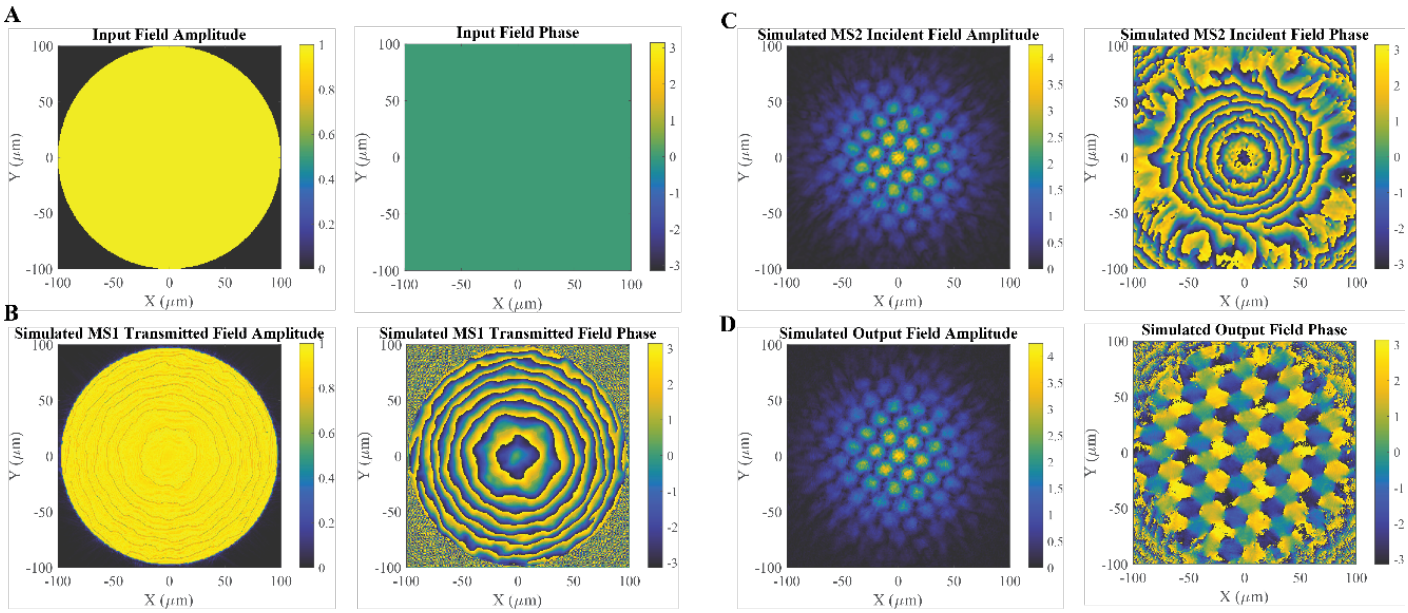

Figure S9: FDTD simulation results of the beam-former and splitter meta-optic example with three beams. (A) The input field distribution to the meta-optic is a circular, uniform distribution. (B) The simulated transmitted field from metasurface 1 exhibits the desired phase shift with a high transmission magnitude. (C) The transmitted field from metasurface 1 is numerically propagated to the plane containing metasurface 2. At this plane, the desired amplitude distribution is formed, but the phase is incorrect. (D) The simulated transmitted field from metasurface 2. This field accurately matches the desired output field distribution, indicating that the meta-optic should perform as expected.

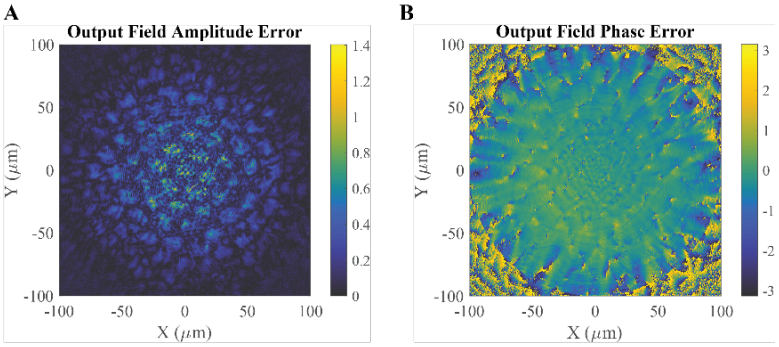

Figure S10: Output field error of the three-beam meta-optic. The amplitude and phase distribution error of the simulated output field relative to the desired output field is low for the three-beam former and splitter example, showing the accuracy of the meta-optic performance. (A) The amplitude error is shown as the root-mean-square error. (B) The phase error of the simulated output field.

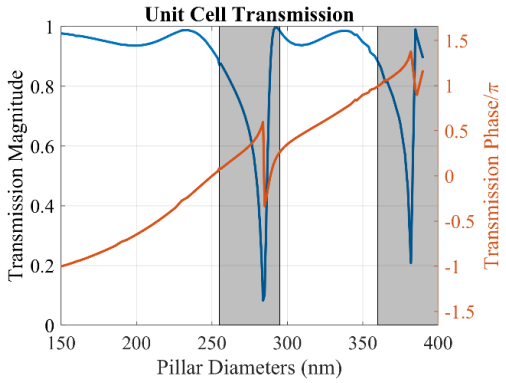

Figure S11: Unit cell transmission characteristics for the $\lambda_0 = 1.1\mu$m implementation of the point-source hologram meta-optic. For this unit cell design, the period is 400nm, the pillar height 750nm, and the pillar diameter ranges from 150nm-360nm while skipping the 255nm-290nm range due to low transmission.

3.3 Point-source Three-dimensional Hologram

The first three-dimensional hologram example forms a constellation of point sources. The point sources trace the outline of the University of Michigan and Vanderbilt University logos, tilted in space to provide depth. Each logo was tilted 15 degrees about its center. The meta-optic output field was constructed by propagating the field from each point source to the meta-optic output plane and summing them together. The complex conjugate of this field profile was used as the desired output field distribution, so the hologram was formed beyond the meta-optic (the observer side of the output plane). The operating wavelength of this example is $\lambda_0 = 1.1\mu$m, with the unit cell transmission characteristics shown in Figure S11.

The amplitude and phase distributions of the meta-optic output field forming the point source hologram are shown in Figure S12(a, b). The metasurface transmission phase profiles are shown in Figure S12(c, d).

The meta-optic was simulated, with results given in Figure S13. Comparing the simulated output field in Figure S13(d) to the desired output field in Figure S12(a, b), we see that the meta-optic design accurately performs the desired complex-valued field conversion. This is further verified in Figure S14 when observing the amplitude and phase error distribution of the simulated output field.

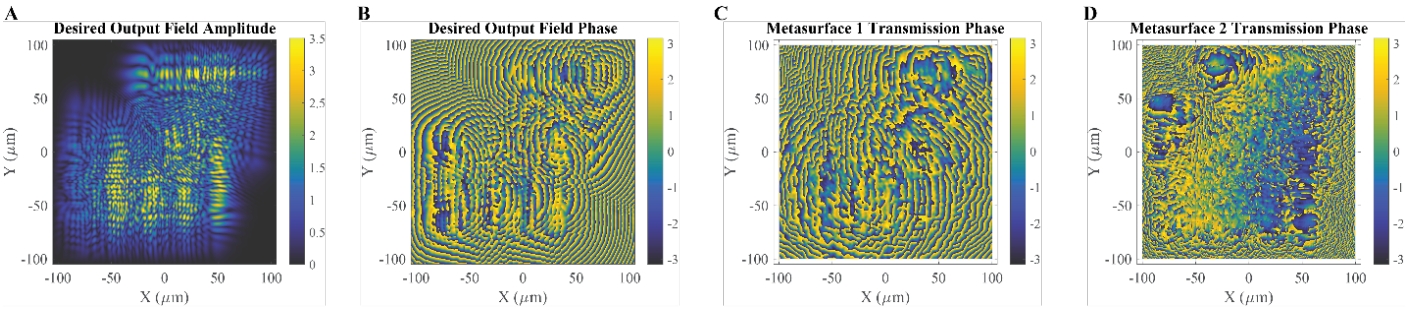

Figure S12: Design of the point source hologram meta-optic. (A, B) The amplitude and phase distributions of the desired output field, which is the complex conjugate of the interference pattern formed by the point sources in the hologram. (C, D) The transmission phase shift profiles implemented by each metasurface to form the desired output field from the uniform, square illumination.

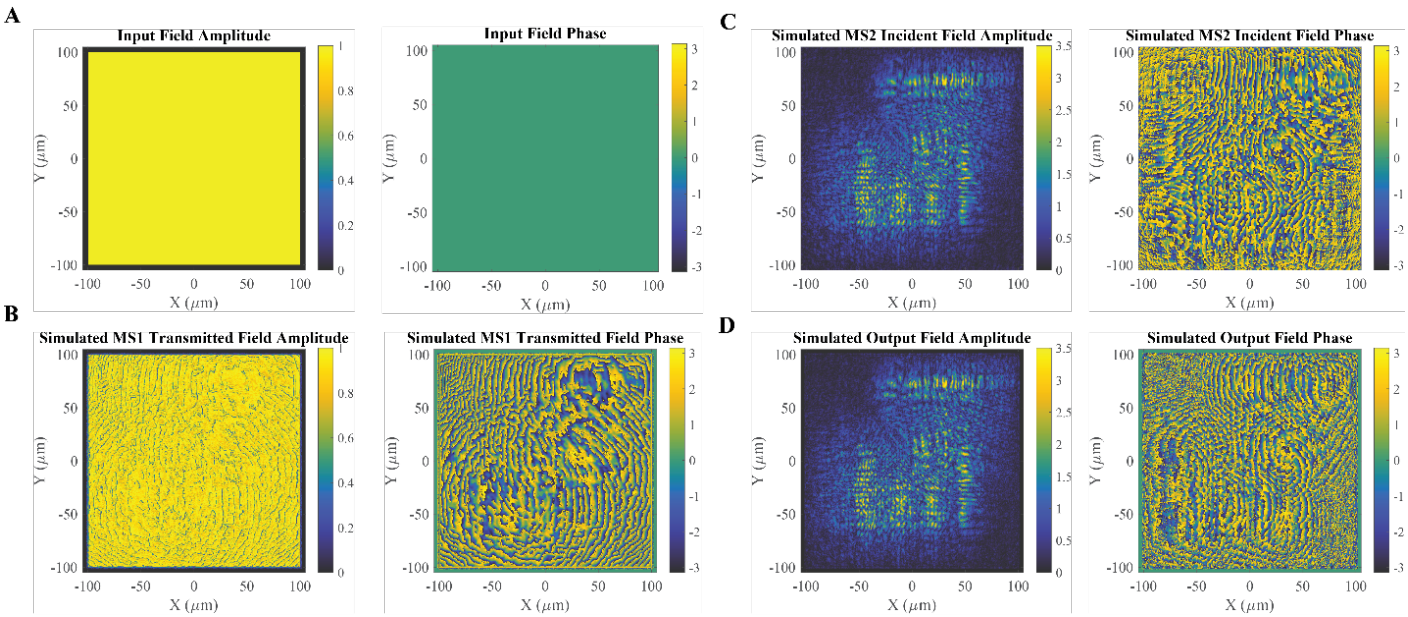

Figure S13: FDTD simulation results of the point source hologram meta-optic example. (A) The input field distribution to the meta-optic is a square, uniform distribution. (B) The simulated transmitted field from metasurface 1 exhibits the desired phase shift with a high transmission magnitude. (C) The transmitted field from metasurface 1 is numerically propagated to the plane containing metasurface 2. At this plane, the desired amplitude distribution is formed, but the phase is incorrect. (D) The simulated transmitted field from metasurface 2. This field accurately matches the desired output field distribution, indicating that the meta-optic should perform as expected.

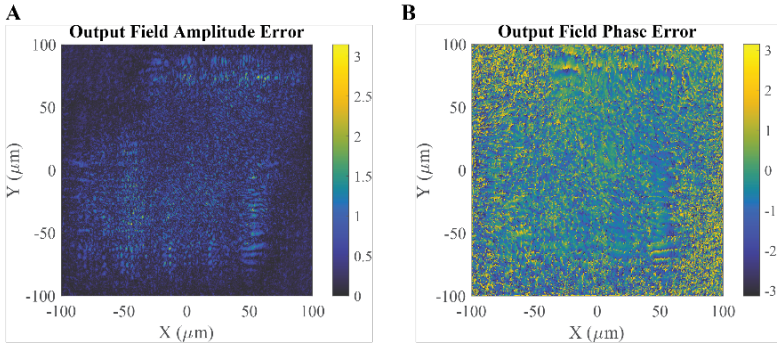

Figure S14: Output field error of the point-source hologram meta-optic. The amplitude and phase distribution error of the simulated output field relative to the desired output field is low for the point-source hologram example, showing the accuracy of the meta-optic performance. (a) The amplitude error is shown as the root-mean-square error. (b) The phase error of the simulated output field.

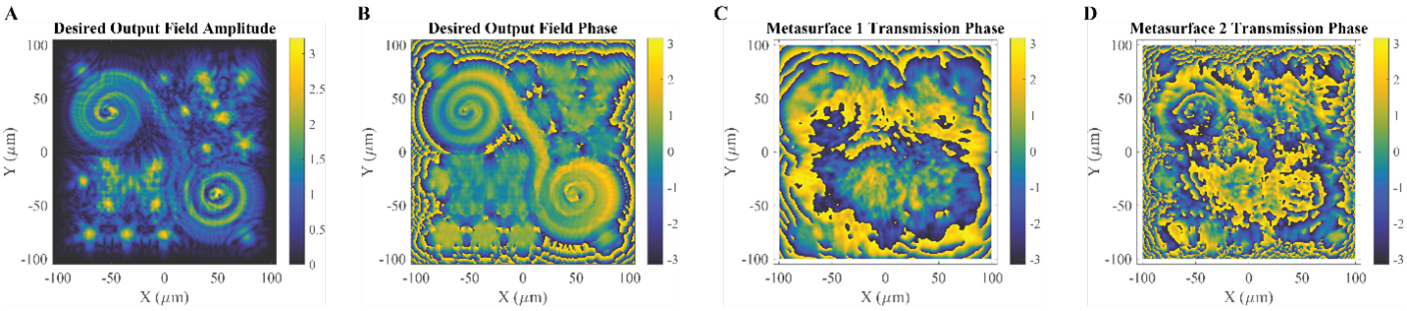

Figure S15: Design of the solid-image 3D hologram. (A, B) The amplitude and phase distributions of the desired output field, which is constructed using computer-generated hologram methods. (C, D) The transmission phase distributions implemented by each metasurface to form the desired output field distribution from a square, uniform illumination.

3.4 Solid-image Three-dimensional Hologram

The second three-dimensional hologram example forms a hologram consisting of solid images tilted in space to provide depth to the scene. The hologram was constructed using computer-generated hologram methods [9, 10, 11]. Each image component was converted to an equivalent source of light, rotated in space to appear at an angle to the observer, and assembled to form the overall scene. This hologram is composed of four separate image components: i) spiral, ii) series of stars, iii) University of Michigan logo, and iv) Vanderbilt University logo. The image components are rotated around an axis and placed at specific coordinates to assemble the 3D scene. The axis of rotation, rotation angle, and center position for each component are given in Table S1. While this 3D scene is relatively simple, the process can be followed to form a scene with many different image components arranged to form three-dimensional shapes of more complex objects.

The field distribution forming these hologram image components is calculated at the meta-optic output plane (located at $z = 0$) and is shown in Figure S15(a, b) as the amplitude and phase distributions. The metasurface transmission phase profiles needed to perform the complex-valued field conversion are shown in Figure S15(c, d).

The meta-optic was simulated, with results given in Figure S16. By comparing the simulated output field in Figure S16(d) to the desired output field in Figure S15(a, b), we see that the meta-optic design accurately performs the desired complex-valued field conversion. This is verified in Figure S17 when observing the amplitude and phase error distribution of the simulated output field.

Table S1: Parameters of each image component to assemble the three- dimensional hologram scene.

Image Component	Rotation Axis	Rotation Angle (degrees)	Center Position
Spiral	$y = x$	20	(0, 0, 104μm)
Stars	No Rotation	No Rotation	(0, 0, 104μm)
University of Michigan Logo	y	25	(-35μm, -35μm, 156μm)
Vanderbilt University Logo	x	25	(55μm, 50μm, 156μm)

Supplemental Video 1: The supplementary media 1 shows a video of the measured three-dimensional hologram intensity as the imaging system focal plane is scanned through the hologram volume. A diagram shows the location of the focal plane within the three-dimensional hologram.

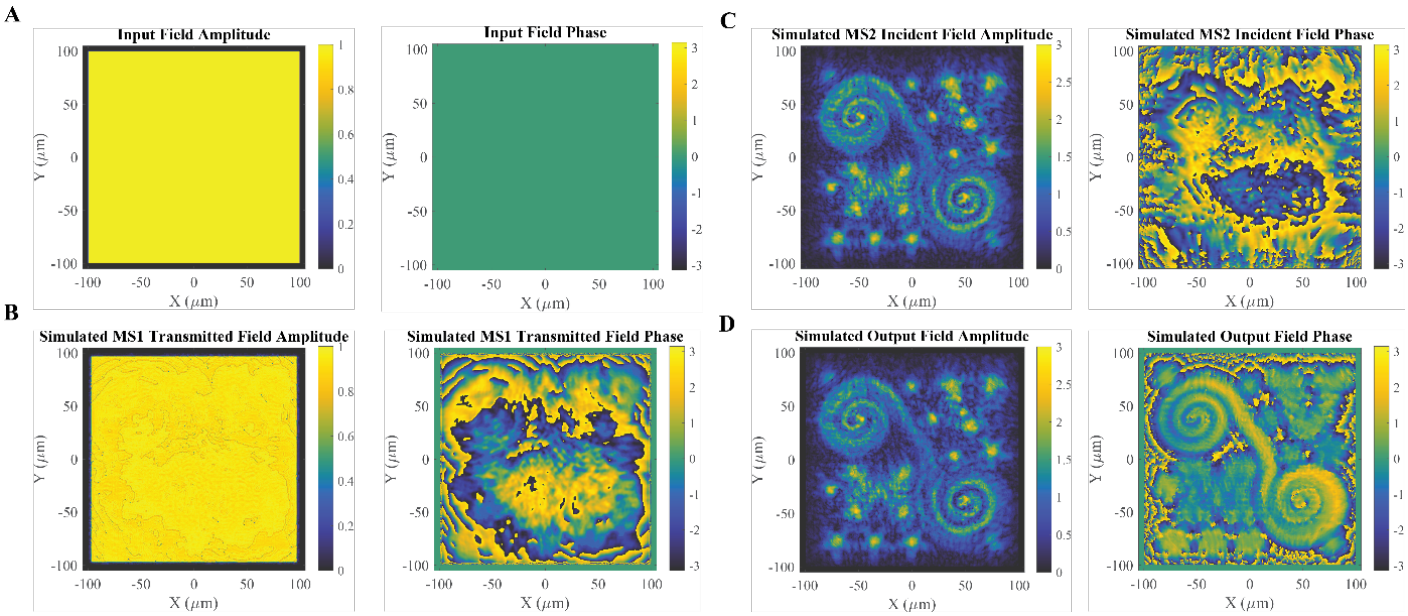

Figure S16: FDTD Simulation results of the solid-image 3D hologram example. (A) The input field distribution to the meta-optic is a square, uniform distribution. (B) The simulated transmitted field from metasurface 1 exhibits the desired phase shift with a high transmission magnitude. (C) The transmitted field from metasurface 1 is numerically propagated to the plane containing metasurface 2. At this plane, the desired amplitude distribution is formed, but the phase is incorrect. (D) The simulated transmitted field from metasurface 2. This field accurately matches the desired output field distribution.

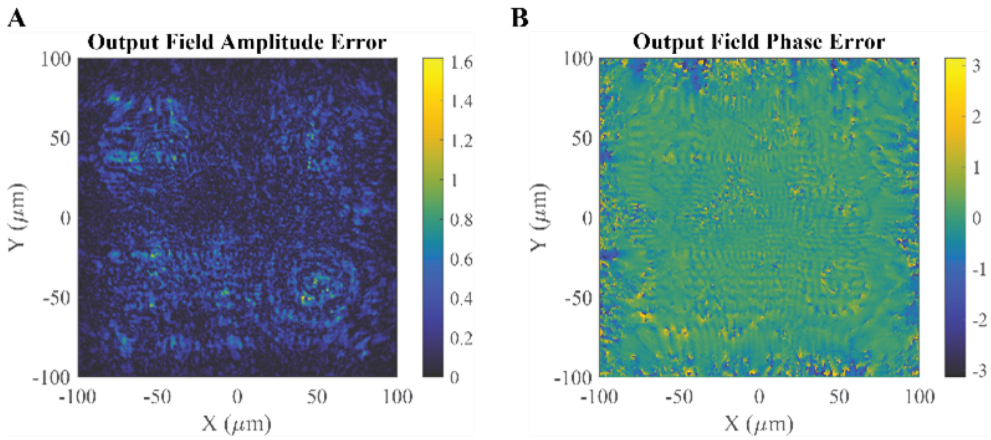

Figure S17: Output field error of the solid-image hologram meta-optic. The amplitude and phase error of the simulated output field relative to the desired output field is low for the solid-image 3D hologram example, showing the accuracy of the meta-optic performance. (A) The amplitude error is shown as the root-mean-square error. (B) The phase error of the simulated output field.

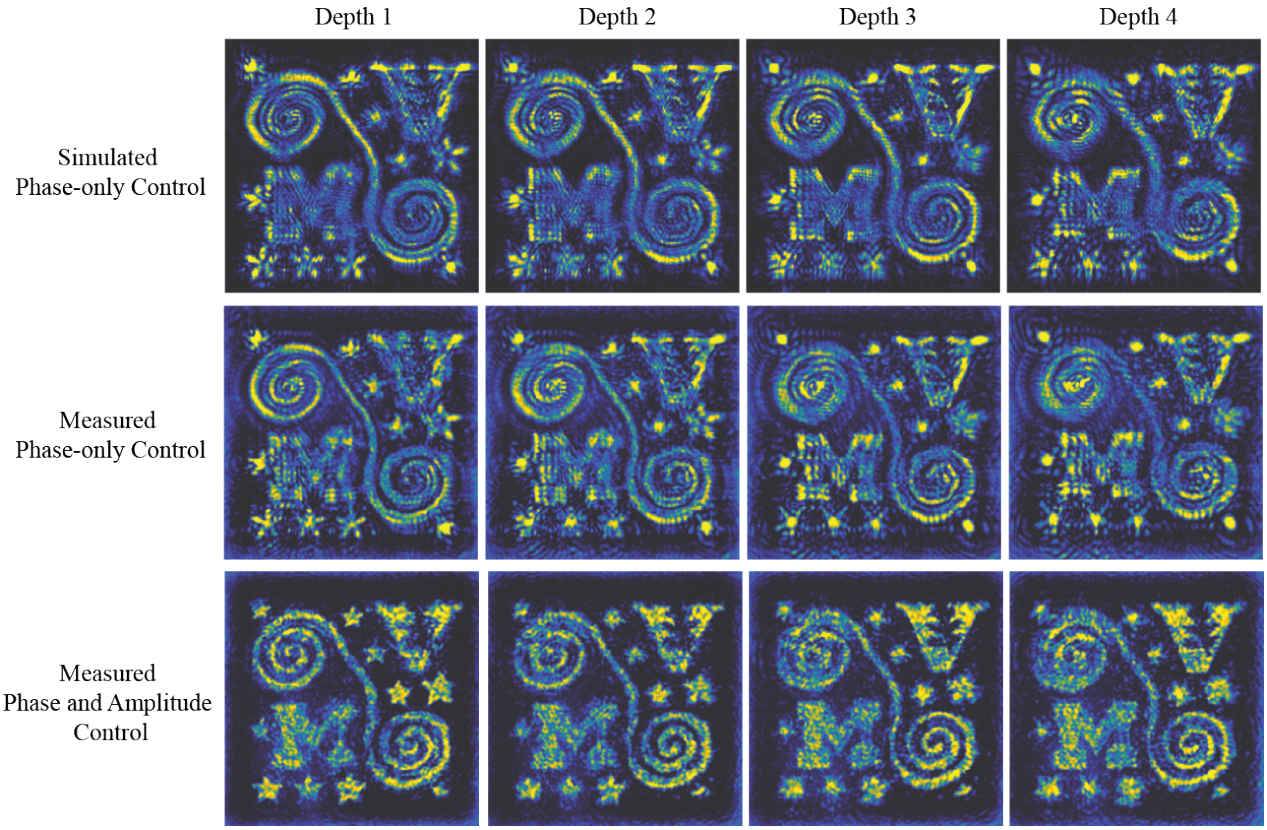

Figure S18: Comparison of hologram images for simulated and measured phase-only control to the measured phase and amplitude control approach. Using both phase and amplitude control results in hologram images that have improved image quality throughout the volume of the three-dimensional hologram.

Supplementary Note 4: Three-Dimensional Hologram — Comparison of Complex-Valued to Phase-only Design

Here, we compare phase and amplitude control provided by the meta-optic to the phase-only control available from a single metasurface. Phase-only control is achieved by an individual metasurface applying a desired phase profile to the incident uniform illumination. The resulting transmitted field exhibits the desired phase profile, but an incorrect amplitude profile. An in-depth comparison of phase-only to complex-valued phase and amplitude control is given by A. Overvig et. al [12].

In the case of the solid-image three-dimensional hologram, the phase-only metasurface was designed to implement the phase distribution of the desired output field profile, shown in Figure S15(b). As the transmitted field distribution propagates away from the metasurface, it forms a version of the desired hologram image. Figure S18 shows the hologram intensity at different depths for the cases of simulated and measured phase-only control compared to measured phase and amplitude control. From this comparison, we see that the measured holograms exhibit higher image quality when both the phase and amplitude profiles of the field distribution are manipulated to match the desired distribution.

References

[1] P. Kovesi, *arXiv* **2015**.

[2] C. Pfeiffer, A. Grbic, *Applied Physics Letters* **2013**, *102*, 23 231116.

[3] R. Pestourie, C. Pérez-Arancibia, Z. Lin, W. Shin, F. Capasso, S. G. Johnson, *Optics Express* **2018**, *26*, 26 33732.

[4] M. Barrow, J. Phillips, *Optics Letters* **2020**, *45*, 15 4348.

[5] S. S. Wang, M. G. Moharam, R. Magnusson, J. S. Bagby, *Journal of the Optical Society of America A* **1990**, *7*, 8 1470.

[6] K. Koshelev, A. Bogdanov, Y. Kivshar, *Optics and Photonics News* **2020**, *31*, 1 38.

[7] A. F. Oskooi, D. Roundy, M. Ibanescu, P. Bermel, J. D. Joannopoulos, S. G. Johnson, *Computer Physics Communications* **2010**, *181*, 3 687.

[8] B. O. Raeker, A. Grbic, *Physical Review Applied* **2021**, *15*, 5 054039.

[9] K. Matsushima, *Applied Optics* **2005**, *44*, 22 4607.

[10] K. Matsushima, S. Nakahara, *Applied Optics* **2009**, *48*, 34 H54.

[11] K. Matsushima, H. Nishi, S. Nakahara, *Journal of Electronic Imaging* **2012**, *21*, 2 023002.

[12] A. C. Overvig, S. Shrestha, S. C. Malek, M. Lu, A. Stein, C. Zheng, N. Yu, *Light: Science and Applications* **2019**, *8*, 1 2047.